EOS MLS Cloud Ice Measurements and Cloudy-Sky Radiative Transfer Model

Dong L. Wu, *Member, IEEE*, Jonathan H. Jiang, and Cory P. Davis

***Abstract*—A cloud ice retrieval technique is described here using measurements at frequencies near 118, 190, 240, and 640 GHz and 2.5 THz from the Earth Observing System Microwave Limb Sounder on the NASA Aura satellite. Measurement principles, methods for cloud detection, and radiative transfer models for retrieving cloud properties are discussed. The 240-GHz data from high-tangent heights are used to retrieve ice water content at pressures $<$215 hPa, and the 118-, 190-, 240-, and 640-GHz radiances from low-tangent heights are used to retrieve ice water paths with different penetration depths. Some early Microwave Limb Sounder (MLS) results are highlighted, and the observed cloud signatures are consistent with the expectation from model simulations, in general. The simultaneous measurements from MLS 240 and 640 GHz radiometers contain useful information on particle sizes. There are significant cloud-induced radiances at 2.5 THz, despite strong attenuation from the atmosphere. Cloud-scattering signatures are polarized at 122 GHz, but the polarization differences are typically less than 10% of the total cloud-induced radiance.**

***Index Terms*—Ice water content (IWC), limb sounding, microwave, polarization, satellite, upper-tropospheric clouds.**

I. INTRODUCTION

CLOUDS play important roles in Earth's dynamical, hydrological, radiative, and chemical processes [1]–[4]. Despite terabytes of satellite cloud imagery, our understanding of cloud properties and distributions remains limited, especially on ice clouds in the upper troposphere. For example, one of the key cloud variables, ice water content (IWC), is difficult to measure from space. Visible/IR techniques are only sensitive to the uppermost cloud layer and often saturated by dense clouds, whereas low-frequency microwave sensors are insensitive to most ice clouds in the upper troposphere (UT). To overcome both penetration and sensitivity limitations, high-frequency microwave radiometry is a promising technique for observing ice clouds in UT.

Remote sensing of ice clouds with passive microwave radiometers is a relatively new research area. Several studies attempted to retrieve cloud ice water path (IWP) based on cloud scattering signatures in nadir-viewing radiances [5]–[10]. Combined radar-radiometer approaches can further improve cloud ice measurements with better vertical resolution, but the retrieved IWC profiles are limited by radar sampling and coverage [11].

This paper describes a technique of measuring cloud ice with the Earth Observing System Microwave Limb Sounder (EOS MLS) on Aura (launched on July 15, 2004). Clouds produce unique signatures in limb sounding geometry, and principles for retrieving cloud ice with limb sounding are somewhat different from those with nadir sounding. For EOS MLS, the high-frequency narrow beamwidth receivers can achieve better vertical resolution and sensitivity than nadir sounding [12], [13]. Cloud scattering-induced signatures are greatly enhanced with limb viewing. For example, a 1-km cloud layer at 16 km with $\mathrm{IWC} = 0.1\ \mathrm{g/m^3}$ will induce about -3 K radiance depression at 233 GHz for nadir viewing, but it can create -65 K depression at limb. The radiative transfer (RT) for limb sounding is much simpler than one for nadir sounding, involving only the atmosphere and clouds. These advantages make limb detection of UT clouds more reliable and accurate than with nadir sounding. However, the horizontal resolution of limb sounding is generally much poorer than nadir sounding.

EOS MLS can observe cloud signatures, or cloud-induced radiances (*Tcir*), in all of its seven radiometers (118 GHz–2.5 THz). These *Tcir* are used to deduce cloud ice in UT, including IWC and horizontal ice water path (hIWP) along the instrument line-of-light (LOS) (Fig. 1). IWC can be retrieved from high-tangent height (h_t) radiance measurements from a window channel. The MLS IWC represents an average over the instrument field-of-view (FOV), which is a volume of $\sim 200 \times 7 \times 3\ \mathrm{km}^3$ in the along-track, cross-track, and vertical dimensions. The hIWP is retrieved from low-h_t measurements using multiple frequencies that have different penetration depths. Each hIWP represents a nearly horizontal column in the LOS direction with a small elevation angle of $\sim 3°$. In most cases, the MLS hIWP column does not reach the surface due to strong atmospheric absorption along the limb path, but, in the polar regions, where air is often dry, the low-h_t radiances may reach the surface.

The IWC retrieval technique using high-h_t radiances has previously applied to Upper Atmosphere Research Satellite (UARS) MLS 203-GHz data, from which the 100-hPa IWC was derived for the period of 1991–1997 [14]. This paper extends this cloud-observing technique to EOS MLS frequencies. This paper first discusses cloud characteristics of EOS MLS radiances in Section II, followed by a description of the cloudy-sky

Manuscript received April 29, 2005; revised October 14, 2005. This work was supported in part by the Jet Propulsion Laboratory, California Institute of Technology, under contract with the National Aeronautics and Space Administration (NASA), and in part by the Aura project.

D. L. Wu and J. H. Jiang are with the Jet Propulsion Laboratory, California Institute of Technology, Pasadena, CA 91109 USA (e-mail: dong.l.wu@jpl.nasa.gov; jonathan.h.jiang@jpl.nasa.gov).

C. P. Davis is with the Institute of Atmospheric and Environmental Science, School of GeoSciences, University of Edinburgh, Edinburgh EH9 3JZ, U.K. (e-mail: cdavis@staffmail.ed.ac.uk).

Digital Object Identifier 10.1109/TGRS.2006.869994

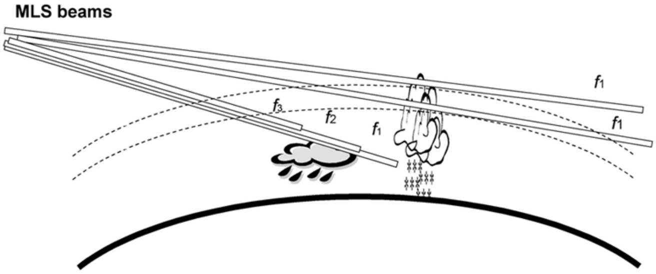

Fig. 1. Cloud ice observations in limb viewing geometry. At high-tangent heights, where radiation can penetrate through the limb at window channels, single-frequency radiances are used to retrieve IWC at pressures <215 hPa. At low-tangent heights, where limb radiation cannot penetrate through the limb, multiple-frequency radiances with different penetration depths can be used to infer hIWP along the LOS.

RT model in Section III. Initial MLS cloud observations are highlighted in Section IV.

II. EOS MLS CLOUD MEASUREMENTS

A. *EOS MLS Experiment*

EOS MLS is a passive instrument with seven radiometers at frequencies near 118, 190, 240, and 640 GHz and 2.5 THz [12], [13]. There are dual polarizations for the 118-GHz and 2.5-THz radiometers. Except for the 118-GHz radiometer, all are double-sideband receivers, which means that the measured radiance is a sum of radiation from two sidebands. Key parameters of MLS radiometers are listed in Table I. The GHz and THz systems have separate antennas but are synchronized in sampling such that they both produce 240 scans, or major frames (MAFs), in an orbit. Each MAF is further divided to 148 minor frames (MIFs) with $1/6$s in a MIF. Unlike step-scanning with UARS MLS, EOS MLS scans continuously in tangent height from the surface to $\sim$92 km in 24.7 s. Two adjacent scans are separated by $\sim$165 km in distance. Aura flies on a sun-synchronous orbit with the $\sim$1:40 pm ascending crossing time, and the MLS latitude coverage is from 82°S to 82°N. Excluding instrument calibration, each MAF contains $\sim$120 MIFs for atmospheric measurements. In the nominal operation [15], the GHz radiometers have $\sim$42 MIFs dedicated to tropospheric observations (separated by $\sim$300 m in h_t), whereas the THz scan has only $\sim$7 MIFs at $h_t < 18$ km [16].

B. *Radiance Uncertainties*

MLS radiance uncertainty consists of spectrally-flat (correlated in frequency) and random components. The spectrally flat uncertainty has little impact on the quality of gas measurements that are mostly based on spectrally varying radiances. However, the cloud measurements depend on the accuracy of absolute radiance calibration. Noise characteristics and calibration issues are detailed in [15] and [16], where the radiance accuracy can be affected by several factors, including errors in baseline, gain, and sideband ratio. The baseline is a spectrally flat component that may come from antenna's ohmic emissions and spillovers. It can be removed effectively on a MAF-by-MAF basis using the measurements at $h_t > 85$ km [15]. The gain error may come from the unmodeled sidelope/spillover radiation. The radiometer sideband ratios are measured during prelaunch testing to accuracy of 0.5%–2% that is radiometer dependent. The total MLS radiance error can be expressed in variance

TABLE I
CHARACTERISTICS OF THE EOS MLS RADIOMETERS

MLS Radiometer[a] (frequency range in GHz)	Polarization 0° = V pol 90° = H pol	Estimated Min. Unc.[b] (K)	Vertical FOV[c] (km)	Cross-Track FOV[c] (km)
R1A (115-122)	0° ± 0.5°	0.3	5.8	12
R1B (115-122)	90° ± 0.5°	0.5	5.8	12
R2 (178-184, 200-207)	0° ± 0.5°	0.3	4.2	8.4
R3 (230-237, 243-250)	90° ± 0.5°	0.2	3.2	6.4
R4 (625-637, 649-661)	90° ± 0.5°	~2	1.4	2.9
R5H (2501-2515, 2531-2544)	~113°	~4	2.1	2.1
R5V (2501-2515, 2531-2544)	~23°	~3	2.1	2.1

a) The two frequency ranges in R2, R3, R4, R5H and R5V indicate the receiver's double-sideband coverage although radiances from two sidebands are inseparable in the radiometric measurements. R1A and R1B are single sideband radiometers with orthogonal polarizations.
b) MLS radiance uncertainty contains frequency-correlated and random components. The latter can be reduced by averaging radiances with more frequency channels from the radiometer. However, the correlated component cannot be reduced by averaging. The minimum value of radiance uncertainties in this column is estimated with a substantial frequency averaging.
c) Both vertical and horizontal FOVs are estimated at $h_t = 1$ km.

$$\sigma^2 = \sigma_{\mathrm{fc}}^2 + \sigma_r^2 \tag{1}$$

where the random component σ_r^2 is proportional to the inverse of the product of bandwidth and integration time. This random noise can be averaged down by using more channels (i.e., more bandwidth). However, the coherent component σ_{fc}^2 *cannot* be averaged down and becomes a fundamental limitation to MLS cloud detection. Especially for the 640-GHz and 2.5-THz measurements, such error can be as large as $\sim$2 K and 3–4 K (Table I), respectively.

C. *Cloud-Induced Radiances (Tcir)*

The MLS spectral filters are chosen to cover spectral emission lines of atmospheric gases (O_2, O_3, H_2 O, N_2O, HNO_3, ClO, etc.). However, the frequencies most useful for cloud measurements need to be away from these spectral lines, the so-called window channels, such that the clear-sky and cloudy radiances can be better separated. Two criteria are used to choose the best window channels in each radiometer: 1) the lowest radiance at upper tropospheric h_t in that radiometer and 2) the least correlation with the abundance of molecules to which the radiometer is sensitive. Radiances from the window channels are a strong function of pointing and water vapor loading due to continuum emissions. For the 640-GHz measurements, O_3 and HNO_3 contributions (2–10 K) are present in almost all the MLS channels. Hence, accurate H_2O, O_3, and HNO_3 profiles are also important for cloud detection.

Tcir is the fundamental quantity in MLS cloud measurements, and is defined as the difference between the measured radiance and the expected clear-sky background. The clear-sky background, which directly affects *Tcir* accuracy, can be determined from nearby observations or from model calculations. The methods for estimating the clear-sky background will be discussed in the next section.

Fig. 2 shows an example of the EOS MLS measurements, where clouds can increase or reduce radiances from the clear-sky background depending on the tangent height where the radiance is measured. At high h_t, where the radiance can penetrate through the limb, *Tcir* is positive as clouds induce more radiation in addition to the clear-sky background. Both emission and scattering of ice particles are important for producing positive *Tcir* at high h_t, especially at frequencies $>$100 GHz. The relative importance between emission and scattering contributions depends on particle sizes, and, therefore, particle microphysical properties are critical for deducing IWC. In order to model the *Tcir*-IWC relations, we make some key assumptions about the model clouds, including spherical homogeneity and cloud type (e.g., thick cirrus anvil). The modeled *Tcir* at a high-tangent height h_t is approximately proportional to IWC at the altitude near h_t. The model *Tcir*-IWC relations vary only slightly with cloud type. Therefore, we may use the modeled *Tcir*-IWC relations to deduce IWC directly from the high-h_t *Tcir*.

At low h_t, where MLS radiances often cannot penetrate through the limb, *Tcir* shows strong dependence on cloud position as well as cloud ice column (i.e., hIWP). In this case, cloud position along the LOS is critical because of the screening effect from clear-sky absorption, whereby absorption in front of clouds can reduce the *Tcir* created by clouds in behind. The screening effect is clearly evident in the observed radiance spectra (Fig. 2) where clouds make the radiance spectra at $h_t = 4.7$ km (gray lines) look like those at a higher h_t. The spectral line (e.g., O_3) features arise in cloudy radiances because radiation near line centers comes mostly from the air above the cloud top and, hence, is less affected by cloud scattering than those at the window channels. The cloud scattering layer acts as a lossy reflector in the upper troposphere that can redirect radiation to the MLS LOS direction. Because cloud scattering is not considered in the current operational model [17], cloudy radiances are either excluded or weighted less in MLS gas retrievals [18].

D. Methods for Determining Tcir

The methods used to obtain *Tcir* can be categorized as either empirical or RT model based. The empirical approach takes advantage of differences between clear and cloudy-sky variabilities (e.g., different spatial/temporal scales) to discriminate these components. The RT model approach computes clear-sky radiances and interprets the radiance difference from calculated clear sky as *Tcir*. The empirical approach is simple and fast to implement, generally performing well in the tropics where atmospheric clear-sky variability is small. The RT model approach is better in coping with situations of large atmospheric variations (e.g., planetary waves), but it is computationally costly and affected by errors in auxiliary data (e.g., tangent pressure, temperature, water vapor).

An empirical method, useful for MLS cloud detection, is based on the daily zonal mean radiances averaged over every 10° latitude bin. Since the occurrence of clouds seen by MLS is small (5%–10%), the zonal mean values are usually close to the background clear-sky radiance with the standard deviation dominated by clear-sky variability. To determine the clear-sky background more accurately, this method is refined with an iterative procedure. Outliers are discarded if their values are $>2\sigma$ from the mean in each 10° latitude bin, and the mean is then recalculated for the bin. This discrimination calculation may need to be repeated for 5–10 times before convergence is reached. The finalized zonal means and standard deviations are interpolated back onto the latitude of each individual measurement, and the difference between the measured radiance and the mean yields *Tcir*. These *Tcir* are only significant if they are $>3\sigma$ from the clear-sky mean. The 3σ criterion is necessary to minimize false alarm in cloud detection.

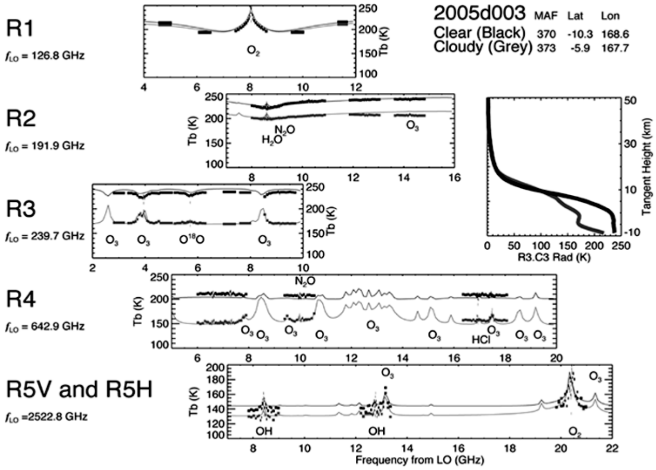

Fig. 2. (Dotted lines) Measured and (continuous lines) modeled radiance spectra for the EOS MLS radiometers at 4.7-km tangent height on January 3, 2005. Black and gray colors are two measurements at a close location, but corresponding to clear and cloudy-sky conditions. The right panel in the middle shows the measured radiance profiles from a 240-GHz window channel, where clouds depress radiances at low-tangent heights, but enhance them at high-tangent heights.

For RT model-based methods, *Tcir* is usually defined as the residual between measured and fitted radiances. Because the model does not have reliable clear-sky information on the cloudy spot, the fitted radiances there are based on either the nearby clear-sky profiles or the *a priori*. In addition, model fits from a broad radiance spectrum (including line features) sometimes produce better estimation of clear-sky radiances at window channels than that from single-channel radiances. Especially at high h_t, fitting the radiances near spectral lines (that are less affected by clouds) makes better determination of the clear-sky radiance at window channels.

III. CLOUDY-SKY RADIATIVE TRANSFER (RT) MODEL

The MLS cloudy-sky model provides key calculations to relate the *Tcir* measurements to cloud ice variables. The model involves complicated RT calculations, which are described in detail in this section.

A. Radiative Transfer Equation

The cloudy-sky RT equation can be expressed as the differential change of radiance with respect to distance interval *ds* in the radio wave propagation direction $\mathbf{n}$

$$\frac{d\mathbf{I}(\mathbf{n})}{ds} = -\mathbf{K}(\mathbf{n})\mathbf{I}(\mathbf{n}) + \mathbf{k}_a(\mathbf{n})B(T) + \oint_{4\pi} \mathbf{P}(\mathbf{n},\mathbf{n}')\mathbf{I}(\mathbf{n}')d\mathbf{n}' \quad (2)$$

where $\mathbf{I} = [I, Q, U, V]^T$ is the Stokes vector in $Wm^{-2}\ \mu m^{-1} sr^{-1}, s$ is the distance along direction $\mathbf{n}$, and B is Planck radiance at air temperature T. $\mathbf{K}(\mathbf{n}), \mathbf{k_a}(\mathbf{n})$, and $\mathbf{P}(\mathbf{n},\mathbf{n}')$ are, respectively, the bulk extinction matrix, absorption coefficient vector, and phase matrix of the scattering medium. These variables represent bulk properties of atmospheric volume, where individual single-scattering properties are multiplied by particle number density and averaged over all orientations and particle types. The argument $\mathbf{n}$ is retained to signify that in general these properties depend on the direction of propagation. The last term in (2) means that each radiation calculation involves the entire radiation field in a scattering medium. A thorough treatment of scattering requires the consideration of polarization, which transforms the RT equation to the vector equation above.

To investigate the influence of clouds on MLS radiances, an independent three-dimensional (3-D) polarized radiance model, atmospheric radiative transfer system (ARTS), is also used for MLS simulations [19]. In this 3-D RT model, a reversed Monte Carlo technique is employed to track back random multiple scattered propagation paths from the sensor to either the emitting point or the entry into the scattering domain. To date, this model has only been used as a reference for comparison to the simplified model described below, and for interpretation of polarized MLS measurements.

B. MLS Cloud-Sky Forward Model

This section describes the cloudy-sky forward model used to calculate MLS cloud retrieval coefficients. Several approximations are made in order to simplify RT calculations.

First, we neglect polarization differences in the radiation, i.e., $\{Q, U, V\} \approx 0$. This reduces (2) to

$$\frac{dI}{ds} = -\beta_e I + \beta_a B(T) + \beta_s J_s \tag{3}$$

where $\beta_e \equiv \beta_{\text{gas\_}a} + \beta_{c\_s} + \beta_{c\_a}$ denotes volume extinction coefficient, which includes contributions from gas absorption ($\beta_{\text{gas\_}a}$), cloud scattering and absorption (β_{c_s} and β_{c_a}). The source function J_s, representing the amount of radiation scattered in by clouds, is an angular integration of radiation over all incident directions.

Using the Rayleigh–Jeans approximation, it is convenient at microwave frequencies to transform radiance to a more measurement-related variable by defining

$$\hat{T} \equiv \frac{c^2}{2k\nu^2} B$$
$$T_b \equiv \frac{c^2}{2k\nu^2} I$$

where $\hat{T}$ and T_b have units of *Kelvin*. T_b is called radiance brightness temperature. Similarly, the scattering source function J_s is replaced by T_{scat}, which is defined as

$$T_{\text{scat}} \equiv \frac{1}{4\pi} \oint P(\Omega, \Omega') T_b(\Omega') d\Omega' \tag{4}$$

where Ω is the direction of radiation coming out of clouds, and Ω' is the direction of incident radiation. The difference between Ω and Ω' is the scattering angle.

Fig. 3 illustrates the geometry for the T_{scat} calculation. The plane-parallel assumption is made to simplify the scattering calculation. As a result, the incident radiance T_b at zenith angle Θ', as a function of θ, ϕ, and Θ, can be reduced to a function of single variable Θ', i.e.,

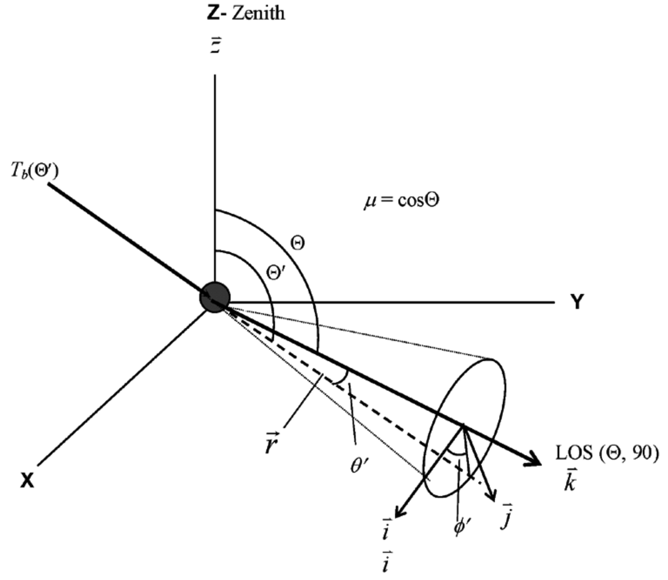

Fig. 3. Diagram illustrating the scattering in a spherical geometry, where the Z axis is at the zenith. The origin is a differential volume containing polydisperse particles, and the LOS lies in the Y–Z plane with an angle Θ with respect to zenith and an angle $\Phi = 90^\circ$ with respect to X. The (θ, ϕ) coordinates are relative to the LOS. ϕ' is the azimuth angle that lies in the plane perpendicular to the LOS.

$$T_{\text{scat}}(\Theta) = \frac{1}{2} \int_0^{\pi} P(\theta') \bar{T}_b(\theta') \sin\theta' d\theta' \tag{4}$$

where

$$\bar{T}_b(\theta') = \frac{1}{2\pi} \int_0^{2\pi} T_b(\Theta') d\phi' \tag{5}$$

and Θ' is related to θ', ϕ' and Θ by

$$\cos\Theta' = \vec{r} \cdot z = \sin\theta' \sin\Theta \sin\phi' + \cos\theta' \cos\Theta. \tag{6}$$

If optical thickness $d\tau = \beta_e \cdot \mu \cdot ds$ (where $\mu = \cos\Theta$) is used instead, (3) can be further reduced to

$$\mu \frac{dT_b(\mu, \tau)}{d\tau} = -T_b(\mu, \tau) + (1 - \omega_0)\hat{T}(\tau) + \omega_0 T_{\text{scat}} \tag{7}$$

where ω_0 is the *single scattering albedo* characterizing the relative importance of scattering and emission. The source function T_{scat} is solved iteratively from (7) at each cloudy location applying the plane-parallel assumption. The iterative T_{scat} calculation proceeds as follows. For a given set of scattering angles, T_{scat} is first computed from (4)–(5) using clear-sky radiances T_b as if there were no clouds. Then, the new T_b is solved by substituting T_{scat} into (7). Because the new T_b may differ from the previous $T_b, T_{\text{ scat}}$ needs to be re-evaluated from the new T_b, leading to the next iteration of solving T_b and T_{scat}. This $T_{\text{scat}} - T_b$ computation chain is repeated several times until convergence (<0.1 K in radiance differences) is found. The number of iterations depends on the disturbance created by cloud scattering; the stronger scattering the more iterations are needed. Once the T_{scat} solution is obtained, the final calculation applies

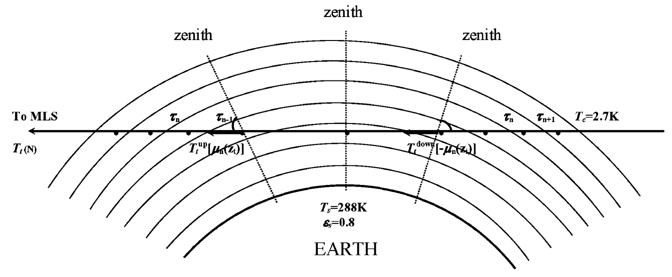

Fig. 4. Geometry for limb-viewing radiative transfer calculations.

(7) along the MLS limb path where all $T_{\rm scat}$ are projected onto the LOS direction (Fig. 4).

C. Polydispersion of Ice Crystals

Cloud volume scattering and absorption coefficients are determined by polydispersion of particles with number density $N(r)$, or particle size distribution (PSD). All cloud particles are assumed to be spheres and $N(r)$ is a function of mass-equivalent particle radius r. The cloud volume extinction and scattering coefficients (β_{c_s} and β_{c_a}) represent the sums over all particles, where single particle extinction and scattering efficiencies (ξ_e, ξ_s) are obtained from the Mie solution. The ice and water permittivities are from an empirical model based on laboratory measurements [21]. Similarly, the phase function of volume cloud scattering in polydispersion is an integration over all particles

$$P(\theta) = \frac{\pi}{\beta_{c\_s}} \int_0^\infty N(r) r^2 \xi_s(r) p(\theta, r) dr \qquad (10)$$

where θ is the scattering angle, and $p(\theta, r)$ is the phase function of single particle from the Mie solution. To link scattering properties to cloud ice, we use the PSD parameterization based on *in situ* measurements [22], which is a function of temperature and IWC. In this parameterized PSD, the dependence of ice density on particle size has been factored in. The MLS RT model divided particle sizes into 40 bins between 0–4000 μm in diameter. IWC, mass-mean diameter ($D_{\rm mm}$), and effective diameter (D_e) can be derived from the PSD.

Ice clouds may have bimodal and height-dependent PSDs in the upper troposphere. Our calculations show that the 240-GHz radiances are mostly sensitive to the large-size mode (~200 μm) in Fig. 5, whereas the 640-GHz radiance is sensitive to both small and large size modes. By comparing MLS observations at these frequencies, one can infer some particle size information about the cloud.

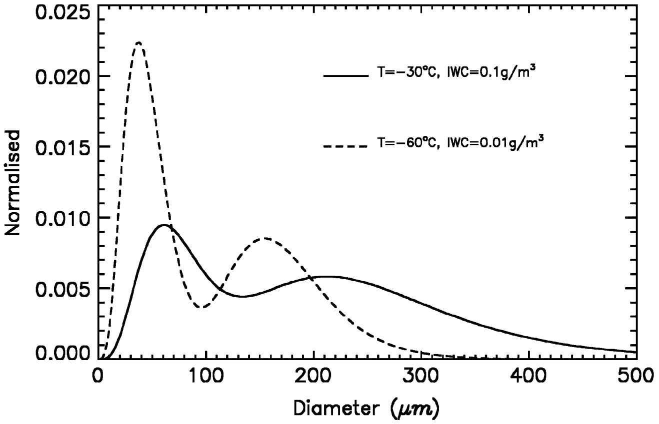

Fig. 5. IWC contributions weighted by the model PSD [22], showing relative importance of different particle sizes. The distributions are normalized such that the area under these curves is unity. These cloud examples represent very different PSDs from the following model parameters: $\mathrm{IWC} = 0.01$ g/m^3 at $-60\,^\circ$C and $\mathrm{IWC} = 0.1$ g/m^3 at $-30\,^\circ$C. The double peaks reflect the bimodal size distributions in the model PSD [22].

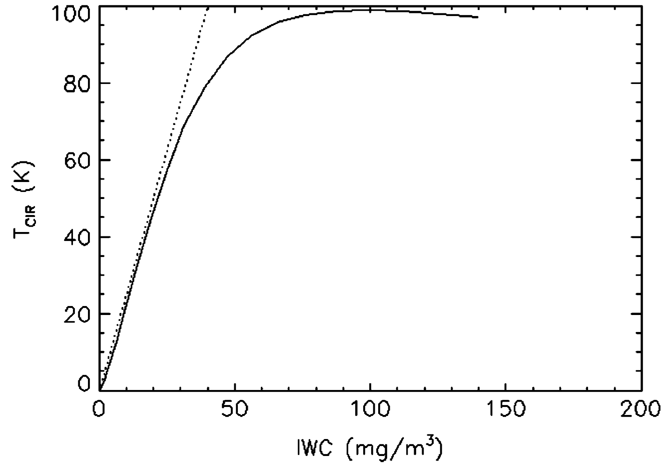

Fig. 6. Modeled *Tcir*-IWC relation for 245-GHz limb radiance at 100 hPa. The dotted line shows the linear portion of the relation with a slope of ~0.4 mg/m^3/K, and the saturation effect is evident at $\mathrm{IWC} >$~50 mg.

TABLE II

CALCULATED COEFFICIENTS FOR THE $Tcir$-IWC RELATIONS AT 215–68 hPa

Ptan hPa	190 GHz	240 GHz	640 GHz
68	0.5	0.40	0.14
83	0.5	0.40	0.14
100	0.8	0.40	0.23
121	1.4	0.43	-
147	1.9	0.61	-
178	-	0.86	-
215	-	1.0	-

D. Modeled Tcir-IWC and Tcir-hIWP Relations

The modeled *Tcir*-IWC and *Tcir*-hIWP relations produce key coefficients to enable fast IWC retrievals. To calculate these coefficients, we assume a 2-km-thick cloud layer with the modeled PSD [22] and the mean tropical temperature profile of CIRA86 (COSPAR International Reference Atmosphere, 1986) [23] as the clear-sky background. At high h_t, where the radiances can penetrate through the atmospheric limb, *Tcir* increases approximately linearly with IWC for values < ~30 mg/m^3 at 245 GHz (Fig. 6) and < ~5 mg/m^3 at 640 GHz (not shown). Table II lists the *Tcir*-to-IWC linear coefficients (mg/m^3/K) calculated by the model, as a function of frequency and tangent pressure.

TABLE III
CALCULATED COEFFICIENTS FOR THE $Tcir$-hIWP COEFFICIENTS AND MAXIMUM MEASURABLE IWP AT SELECTED TANGENT HEIGHTS

Radiometer		Coefficients			Max.
Freq	(GHz)	2km	5km	10km	IWP
R1A	115.3	-360	-410	-690	19
	122.0	-330	-370	-590	16
R2	177.0	-71	-78	-	9.7
	200.5	-46	-51	-	6.7
R3	233.0	-32	-35	-	4.1
	245.4	-28	-30	-	3.4
R4	636.5	-9.0	-9.4	-12	0.16
R5V	2514.8	-0.53	-0.55	-0.58	0.02

More sophisticated *Tcir*-IWC relations, such as nonlinear latitude-dependent coefficients, will be developed in the future. Clouds with very large IWC can deviate from the linear *Tcir*-IWC relation, but these cases represent a very small percentage of MLS cloud measurements.

The cloud ice column measured by MLS, hIWP, is defined by

$$\mathrm{hIWP} \equiv \int_{\mathrm{LOS}} \mathrm{IWC}(s) e^{-\tau_e(s)} ds \tag{11}$$

where $\tau_e(s) = \int_{\mathrm{LOS}}^{s} \beta_e(s') ds'$ is the frequency-dependent optical depth along LOS. The weight $e^{-\tau_e(s)}$ is also known as the transmission function, which determines the percentage of IWC observable by the sensor. By this definition, hIWP excludes the contributions beyond extinction. Because limb sounding has a long LOS path and some channels have strong attenuation from atmospheric gaseous/cloud extinction, it is important to characterize the cloud sensitivity using cloud ice within the penetration depth. The atmospheric attenuation is of general concern in cloud remote sensing even at low microwave frequencies. It becomes less serious in nadir sounding than limb sounding because of shorter path lengths. The hIWP concept introduced here is a more robust quantity for MLS cloud ice measurements than IWP since most MLS channels cannot reach the surface due to strong atmospheric attenuation and cloud self-extinction at limb (Fig. 1). Cloud self-extinction is significant for thick-and-dense clouds, where the front part of clouds may block the radiation of those in the back. hIWP implies that each IWP should be specified by defining the bottom of cloud ice column, which may not be at the surface. For MLS hIWPs retrieved at the window channels near 122, 200, 233, and 636 GHz, the estimated bottoms are ~10, ~7, ~6, and ~10 km, respectively, based on the position where $\tau_e = 1$.

The *Tcir*-to-hIWP relations are calculated using the same clear-sky background and the same PSD, but a different cloud type. The vertical profile of cloud ice is similar to deep convective type, decreasing exponentially with height, but the shape of distribution is fixed in all the simulations. The sensitivity is then calculated by scaling this vertical profile for different cloud ice loadings. The calculated *Tcir*-hIWP coefficients in g/m^2/K and the maximum measurable IWP in kg/m^2 are given in Table III for selected h_t and frequencies.

E. Uncertainties

The quality of MLS IWC and hIWP measurements are affected by radiance and forward model uncertainties. The *Tcir* uncertainty varies from ~2 K at 100 hPa to ~10 K at 300 hPa, depending on the accuracy of clear-sky gas retrievals. This may induce 10%–50% error in IWC, but is mostly random. In the polar regions, where the atmosphere is very dry, MLS radiances at tangent pressures $>$ ~700 hPa can be affected by surface emission/reflection. The polar low-h_t radiances may produce false cloud detections and are, therefore, discarded in this study.

Larger uncertainties are found in the modeled *Tcir*-IWC and *Tcir*-*h*IWP relations, where assumptions on ice cloud microphysics must be made (e.g., particle size and shape). Some of these assumptions are not robust. For example, our model PSD, although based on aircraft observations [22], represents mostly the cases from subtropical cirrus anvils. It may induce large errors when applied to other cloud types such as polar clouds and deep convective cores. Our analyses show that using different PSD parameterizations [24] could induce a scaling difference as large as a factor of ~2 in the deduced IWC.

We conducted a number of sensitivity studies to estimate potential errors in the modeled *Tcir*-IWC relation. In the case of strong updraft, more large ice particles may be lifted to a high altitude than in regular cirrus anvils. For these extreme conditions, we examined the differences in the *Tcir*-IWC relation between the model PSDs at −60 °C and −75 °C, and found mixing these PSDs would yield a ~30% difference in the retrieved IWC with 240-GHz radiances. The difference is larger at 122 GHz because, in this case, the sensitivity shifts to larger particle sizes, away from the 200-μm mode seen in Fig. 5. Furthermore, the model PSD [22] represents an average over measurements sampled at ~1-km resolution. There is large variability around each model PSD. Because MLS cloud measurements are also subject to averaging over a large area, the PSD variability from small-scale sampling is likely to play a secondary role.

We also investigated sensitivity differences due to cloud thickness, and found that the sensitivity can differ by up to 70% between 2-km cirrus anvils and 10-km-deep convective clouds. The sensitivity difference in these simulations is mostly due to stronger cloud self extinction in the deep convective case. Errors due to 3-D cloud structures have yet to be further quantified, which is an undergoing research with the model developed recently by Davis *et al.* [19]. Generally speaking, the single MLS measurement can be complicated by cloud inhomogeneity along the LOS, and, therefore, it is strongly recommended to analyze the data with averaging. For example, weekly or monthly means may be useful for investigating some climatological or synoptic cloud features. According to *in situ* observations, the averaged IWC decreases exponentially with height in UT [22], which allows us to convert MLS *Tcir* directly to IWC at the tangent height where *Tcir* is measured. This simplified relationship may be invalid at pressures $>$250 hPa in the tropics such that an inversion on *Tcir* might be required before it could be converted to IWC [14]. For this reason, MLS IWC should be used only for pressures $<$215 hPa.

Mixed-phase clouds may cause degradation in MLS sensitivity to cloud ice because liquid clouds are much efficient emitter/absorber than ice. Our simulations show that mixing ice clouds with liquid droplets up to $\sim$8 km may induce a 50% error in the modeled *Tcir*-IWC relation at 240 GHz. Again, mixed-phase clouds are not frequent at pressure $<$215 hPa, and, therefore, this type of error is unlikely to have large impacts on the MLS IWC measurements from the high-h_t radiances.

Finally, ice particles with different shapes may induce systematic error as large as a factor of 2 in volume extinction under the extreme conditions (e.g., Hollow Columns and Rosettes) [7]. Because the elongated particles have less volume than spheres, the difference in the *Tcir*-IWP relation was found to be $<$ 50% at 200–300 GHz. In reality, other factors, such as turbulence inside/near clouds, are likely to further reduce polarization differences in the upwelling radiation. Weak polarized scattering signatures in UT clouds are confirmed recently with MLS 122-GHz observations, showing that the polarization differences are $<10\%$ of cloud-induced radiances (i.e., $Tcir$) [20].

IV. MLS V1.5 IWC RETRIEVAL

The v1.5 is MLS first data version made available publicly [13], [18], [25]. The standard IWC product in this version is derived from the 240-GHz measurements where the radiances are affected least by atmospheric gaseous emissions. The two-dimensional clear-sky RT model [17] is used to derive *Tcir*, which is defined as the radiance residuals between measured and fitted clear-sky radiances at the end of each retrieval phase. The cloud flags are based on *Tcir* and re-evaluated at the end of each retrieval phase. The criteria used in the current operational retrieval for cloud flag are relatively loose (i.e., cloudy if *Tcir*$>$10 K or *Tcir*$>$30 K). *Tcir* accuracy usually improves as the gas retrieval progresses in phase.

To keep the level 2 data processing uninterrupted in cloudy-sky conditions, the v1.5 algorithms treat the tropospheric measurements cautiously and seek to update *Tcir* calculations progressively as the gas retrievals improve in phase [18]. In the initial phase, temperature (T) and tangent pressure (P) retrievals are very conservative, *not* using any tropospheric radiance measurements. Thus, the tropospheric T and P profiles from this phase are basically the *a priori* from the operational data provided by Global Modeling and Assimilation Office (GMAO) GEOS-4. Using these initial T and P profiles, the first *Tcir* and cloud flags are estimated by assuming 110% saturation in the troposphere. We still use the flagged radiances in the next H_2O retrieval phase but the precisions of flagged radiances are inflated to 2 K, making them less weighted during the retrieval. After the initial H_2O retrieval, *Tcir* and cloud flags are re-evaluated for each radiometer, followed by a multimolecule retrieval (e.g., T, P, H_2O, O_3, N_2O, and HNO_3). With the updated profiles of these molecules, *Tcir* and cloud flags are finalized for all the radiometers. The flagged radiances are either weighted less or excluded in the subsequent gas retrievals.

Tcir from the v1.5 algorithm may have biases and needs to be screened for better cloud detection. We find that *Tcir* is a strong function of latitude, and we use the screening procedure similar to the iterative method described in Section II-D to remove the biases. Then, the screened *Tcir* is converted to IWC using the modeled *Tcir*-IWC relation in Section III-D. The screening method also provides the standard deviation of clear-sky residuals, which can be used for cloud detection. The threshold for detecting significant IWC varies from 2 mg/m^3 at 100 hPa to $\sim$10 mg/m^3 at 215 hPa, based on the 3σ clear-sky standard deviation. The measurements at wintertime high latitudes are slightly noisier because of stronger wave activity in the upper troposphere and lower stratosphere. Fig. 7 shows an example of MLS IWC distributions at 100, 121, 147, 178, and 215 hPa screened out for January 9–11, 2005.

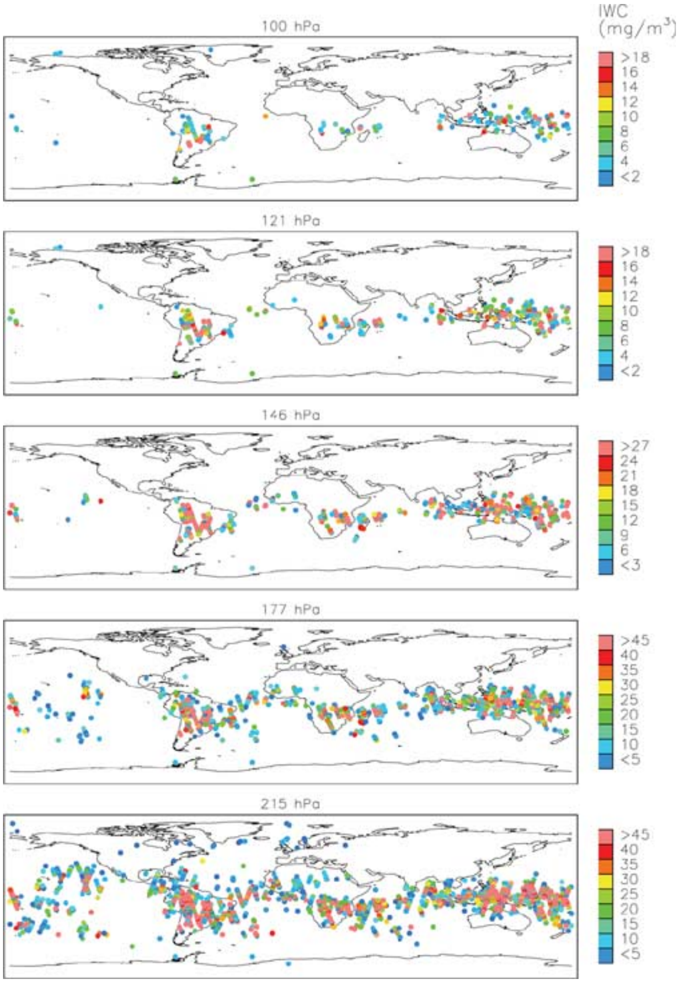

Fig. 7. Composite maps of MLS IWC measurements during January 9–11, 2005. Only IWCs with value >5 mg/m^3 are colored.

An initial comparative study with five global circulation models (GCMs) revealed that MLS IWCs are generally in good agreement with the models [26]. This study was focused on monthly mean distributions of cloud ice in UT for January. The monthly average over large (e.g., $4^\circ \times 8^\circ$ latitude-longitude) grid boxes helps to make comparisons of synoptic features between the models and MLS observations. However, there are large differences among the modeled IWC distributions, indicating a serious gap in our knowledge about UT ice clouds.

V. OTHER EARLY RESULTS FROM MLS

A. MLS 240 and 640 GHz Tcir

Simultaneous measurements from MLS 240- and 640-GHz radiometers can be used to distinguish clouds of different PSDs.

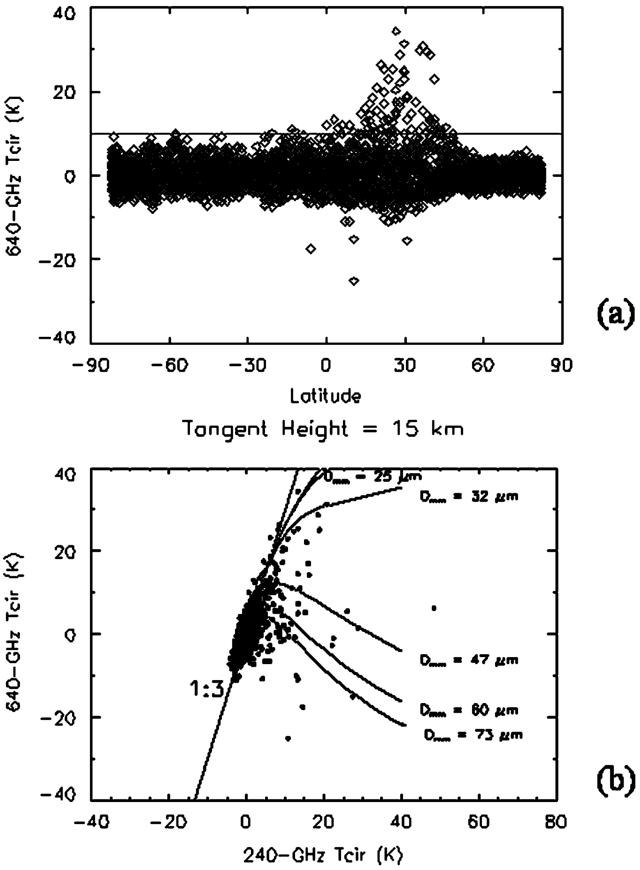

Fig. 8. (a) MLS 640-GHz *Tcir* at 15- km tangent height for August 29, 2004. (b) Correlation between 240- and 640-GHz *Tcir* at 15-km tangent height for the same day. The curves are the model 240:640 GHz relations with various mass-mean diamters D_{mm} labeled on the side.

Fig. 8(a) shows the daily 640-GHz *Tcir* as a function of latitude, which are obtained with the screening method described in Section II-D. In Fig. 8(a), the background clear-sky radiances have been removed. The 640-GHz clear-sky radiances, typically ~140 K at 15-km tangent height, are mainly due to atmospheric continuum radiation. As given in Table I, the 640-GHz radiometer has a relatively large frequency-correlated error, which cannot be averaged down with more bandwidth. Thus, a large threshold (10 K) is used for cloud detection, and it is comparable to the $\sim 3\sigma$ variability of the clear-sky background. At 240 GHz, the clear-sky background is ~20 K with the 3σ variability of ~5 K.

On August 29, 2004, strong enhancements are found in dense cirrus over Asia at altitudes >14 km, which is collocated with high CO concentration measured simultaneously by MLS [26] because polluted aerosols can modify cloud microphysical properties (e.g., PSD). These MLS observations are of great importance to understand indirect effects of polluted aerosols on climate change.

RT calculations [Fig. 8(b)] show that the 240 : 640-GHz correlation is sensitive to cloud PSD. D_{mm} serves as a better parameter than D_e to characterize the PSD differences since D_e varies only slightly among these high clouds. D_e has been widely used in visible/IR cloud retrievals because of the sensitivity to scattering cross section on the uppermost cloud layer. At microwave frequencies, small D_{mm} clouds would produce a 240 : 640-GHz ratio similar to clear-sky measurements because cloud ice emission is the dominant source of *Tcir*. Scattering becomes more important for clouds with large D_{mm}, which makes the 240 : 640-GHz ratio deviate from that with the small D_{mm} clouds.

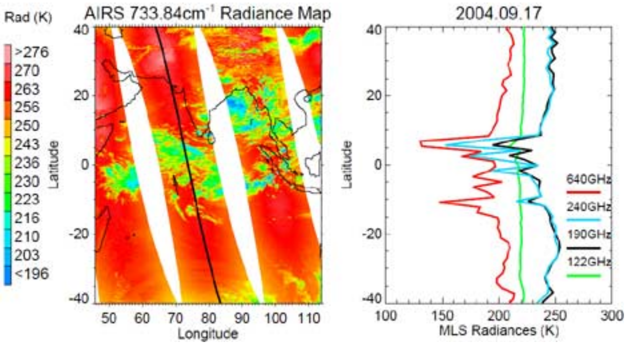

Fig. 9. Example of the A-Train radiances observed by (left) Aqua AIRS and (right) Aura MLS at 4-km tangent height. The straight line in the center of AIRS swath is the MLS measurement track for September 17, 2004. The AIRS channel (733.84 cm^{-1}) has a clear-sky weighting function peaked at ~800 hPa, whereas the MLS weighting functions at 122-, 190-, 240-, and 640-GHz window channels peak at about 170, 270, 270, and 200 hPa, respectively.

At 15-km tangent height, the 640-GHz radiance becomes insensitive to cloud scattering because of the large (~140 K) clear-sky background. Under this background, the amounts of scattered-in and scattered-out radiation are approximately equal, making the net 640-GHz *Tcir* about zero. However, the 640-GHz radiance is still quite sensitive to cloud ice emission, which will not be canceled out, and produces a positive *Tcir* for clouds of small D_{mm}. On the other hand, the 240-GHz radiance is sensitive only to large D_{mm} clouds with clear-sky background of ~20 K at this height. This background gives a broad dynamic range for detecting large IWC. Together, these sensitivity differences provide MLS with a unique ability to distinguish upper-tropospheric clouds of different D_{mm}.

B. MLS and NASAs "A-Train" Measurements

Known for large spatial and temporal variabilities, clouds play a central role in climate change that is difficult to quantify. As part of NASA synergic-observing system, the so-called *A-Train*, Aura is flying in formation with Aqua (launched in 2002), and CloudSat 94-GHz Cloud Profiling Radar (CPR) (due for launch in late 2005) [29] with coincident measurements within ~15 and ~7 min, respectively. Aqua atmospheric infrared sounder (AIRS) [30] and moderate resolution imaging spectroradiometer (MODIS) [31] have high-resolution horizontal coverage at visible and infrared frequencies whereas the CloudSat CPR will profile ice clouds with 0.5-km vertical and 1.4 km × 3.5 km horizontal resolution. Together with these *A-Train* observations, the MLS 118 GHz–2.5 THz radiances can provide new insights on cloud properties and variabilities (Fig. 9).

C. THz Tcir

Despite strong atmospheric continuum absorption at 2.5 THz, the THz spectral windows can penetrate down to the uppermost troposphere and become affected by clouds. Like the 640-GHz

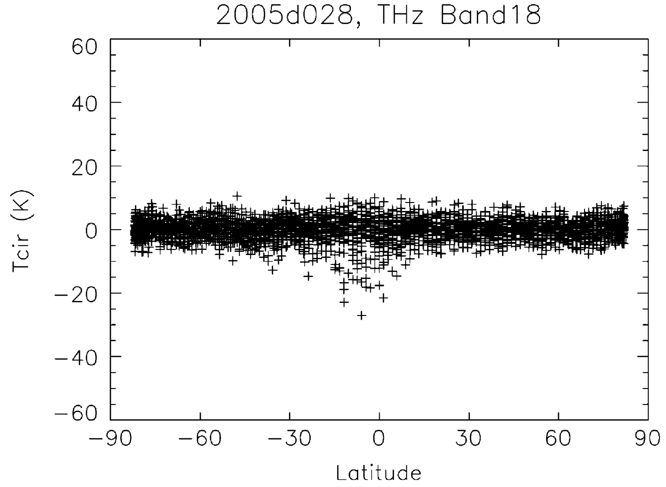

Fig. 10. *Tcir* on January 28, 2005, derived from the band 18 radiances in the 2.5-THz radiometer for $h_t < 5$ km. Cloud scattering causes the observed radiances less than typical clear-sky backgrounds, producing negative *Tcir*, where measurements with *Tcir* < − 10 K indicate the significant presence of clouds.

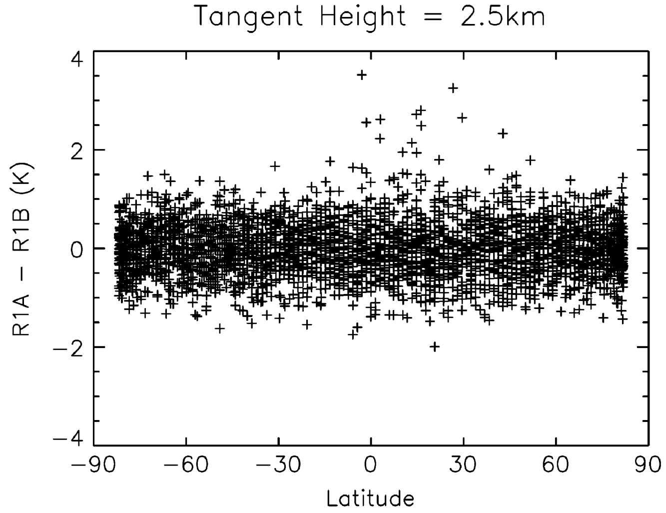

Fig. 11. R1A-R1B radiance differences at a 2.5-km tangent height for August 29, 2004. The positive differences indicate that *Tcir* at 122 GHz are polarized due to preferential orientation of ice crystals. The polarization differences can be as high as 4 K, significantly above the 3σ noise background ($\sim$1.5 K).

radiances, the THz measurements have a relatively large correlated noise that cannot be reduced by frequency averaging. As indicated in Table I, the minimum precision for the THz radiances is $\sim$3–4 K, corresponding to 9–12 K 3σ uncertainty. Such radiometric uncertainty largely limits cloud detection with MLS THz measurements. Nevertheless, as shown in Fig. 10, *Tcir* as large as -30 K are observed due to ice cloud scattering at high altitudes. These tropical *Tcir* reflect a mixture of dense cirrus and deep convective clouds.

D. Polarized Tcir at 122 GHz

The MLS R1A(H) and R1B(V) radiometers have the same frequency channels but with orthogonal polarization. The 122-GHz channel in these radiometers can penetrate down to $\sim$13 km, and *Tcir* as large as -40 K is observed at $h_t < 10$ km. However, as shown in Fig. 11, the polarization differences between R1A and R1B *Tcir* are generally <4 K (or <10% of *Tcir*), which may be interpreted as a result of orientation preference of ice crystals. A detailed analysis and modeling study on the MLS R1A and R1B polarized radiances can be found elsewhere [20].

VI. SUMMARY AND FUTURE WORK

We have described the methods and the model used to derive MLS *Tcir*. These methods continue to be refined as the MLS radiances are better understood. We use realistic PSDs and cloud profiles in the cloudy-sky RT model to derive the *Tcir*-IWC and *Tcir*-hIWP relations, which is used then to retrieve IWC at pressures <215 hPa and the hIWP along MLS LOS at $h_t < 5$ km.

Preliminary results from the EOS MLS indicate that the 240-GHz radiances provide useful IWC measurements. The retrieved UT IWC compares reasonably well with climatologies from several GCMs [26]. In addition, the 240 : 640-GHz measurements exhibit useful information on ice particle sizes of UT clouds. The THz radiances at low h_t are found to be sensitive to cloud scattering despite large noise and atmospheric absorption, and *Tcir* can reach as large as -30 K in the tropics. Significant (3–4 K) polarized cloud radiances are observed at 122 GHz and the polarized signals are generally <10% of total *Tcir*.

The hIWP retrievals are to be implemented in a future MLS algorithm. The MLS channels near the 183.3 GHz water line and the 233.9-GHz $O^{18}O$ line can provide hIWP s with different penetration depths. MLS cloud measurements, together with other A-Train observations, can greatly improve our understanding on global cloud properties and their roles in climate change.

ACKNOWLEDGMENT

The authors would like to thank their MLS colleagues for the instrument operation and data processing, especially Dr. J. Waters, Dr. W. Read, and Dr. M. Filipiak for valuable discussions and comments on this work.

REFERENCES

[1] V. Ramanathan, R. D. Cess, E. F. Harrison, P. Minnis, and B. R. Barkstrom, “Cloud-radiative forcing and climate—Results from the Earth radiation budget experiment,” *Science*, vol. 243, pp. 57–63, 1989.

[2] G. L. Stephens, “Cloud feedbacks in the climate system: A critical review,” *J. Climate*, vol. 18, pp. 237–273, 2005.

[3] B. A. Wielicki, R. D. Cess, M. D. King, D. A. Randall, and E. F. Harrison, “Mission to planet Earth: Role of clouds and radiation in climate,” *Bull. Amer. Meteorol. Soc.*, vol. 76, pp. 2125–2153, 1995.

[4] R. D. Cess *et al.*, “Interpretation of cloud climate feedback is produced by 14 atmospheric general circulation models,” *Science*, vol. 245, pp. 513–516, 1989.

[5] J. Vivekanandan, J. Turk, and V. N. Bringi, “Ice water path estimation and characterization using passive microwave radiometry,” *J. Appl. Meteorol.*, vol. 30, pp. 1407–1421, 1991.

[6] A. J. Gasiewski, “Numerical sensitivity analysis of passive EHF and SMMW channels to tropospheric water vapor, clouds, and precipitation,” *IEEE Trans. Geosci. Remote Sens.*, vol. 30, no. 5, pp. 859–870, Sep. 1992.

[7] K. F. Evans and G. L. Stephens, “Microwave radiative transfer through clouds composed of realistically shaped ice crystals. Part I: Single scattering properties,” *J. Atmos. Sci.*, vol. 52, pp. 2041–2057, 1995.

[8] ——, “Microwave radiative transfer through clouds composed of realistically shaped ice crystals. Part II: Remote sensing of ice clouds,” *J. Atmos. Sci.*, vol. 52, pp. 2058–2072, 1995.

[9] G. Liu and J. A. Curry, “Topical ice water amount and its relations to other atmospheric hydrological parameters as inferred from satellite data,” *J. Appl. Meteorol.*, vol. 38, pp. 1182–1194, 1998.

[10] F. Weng and N. C. Grody, “Retrieval of ice cloud parameters using a microwave imaging radiometer,” *J. Atmos. Sci.*, vol. 57, pp. 1069–1081, 2000.

[11] G. M. Skofronick-Jackson and J. R. Wang, “The estimation of hydrometeor profiles from wideband microwave observations,” *J. Appl. Meteorol.*, vol. 39, pp. 1645–1656, 2000.

[12] J. W. Waters *et al.*, “The UARS and EOS Microwave Limb Sounder experiments,” *J. Atmos. Sci.*, vol. 56, pp. 194–218, 1999.

[13] J. W. Waters *et al.*, “The Earth Observing System Microwave Limb Sounder (EOS MLS) on the Aura satellite,” *IEEE Trans. Geosci. Remote Sens.*, vol. 44, no. 5, pp. 1075–1092, May 2006.

[14] D. L. Wu, W. G. Read, A. E. Dessler, S. C. Sherwood, and J. H. Jiang, “UARS MLS cloud ice measurements and implications for H_2O transport near the tropopause,” *J. Atmos. Sci.*, vol. 62, no. 2, pp. 518–530, 2005.

[15] R. F. Jarnot, V. S. Perun, and M. J. Schwartz, “Radiometeric and spectral performance and calibration of the GHz bands of EOS MLS,” *IEEE Trans. Geosci. Remote Sens.*, vol. 44, no. 5, pp. 1131–1143, May 2006.

[16] H. M. Pickett, “Microwave Limb Sounder THz module on Aura,” *IEEE Trans. Geosci. Remote Sens.*, vol. 44, no. 5, pp. 1122–1130, May 2006.

[17] W. G. Read, Z. Shippony, M. J. Schwartz, N. J. Livesey, and W. V. Snyder, “The clear-sky unpolarized forward model for the EOS Aura Microwave Limb Sounder (MLS),” *IEEE Trans. Geosci. Remote Sens.*, vol. 44, no. 5, pp. 1367–1379, May 2006.

[18] N. J. Livesey, W. V. Snyder, W. G. Read, and P. A. Wagner, “Retrieval algorithms for the EOS Microwave Limb Sounder,” *IEEE Trans. Geosci. Remote Sens.*, vol. 44, no. 5, pp. 1144–1155, May 2006.

[19] C. P. Davis, C. Emde, and R. S. Harwood, “A 3-D polarized reversed Monte Carlo radiative transfer model for millimeter and submillimeter passive remote sensing in cloudy atmospheres,” *IEEE Trans. Geosci. Remote Sens.*, vol. 43, no. 5, pp. 1096–1101, May 2005.

[20] C. P. Davis, D. L. Wu, C. Emde, J. H. Jiang, R. E. Cofield, and R. S. Harwood, “Cirrus induced polarization in 122 GHz Aura Microwave Limb Sounder radiances,” *Geophys. Res. Lett.*, vol. 32, no. 14, 2005. L14806, DOI:10.1029/2005GL022 681.

[21] J. H. Jiang and D. L. Wu, “Ice and water permittivities for millimeter and sub-millimeter remote sensing applications,” *Atmos. Sci. Lett.*, vol. 5, no. 7, pp. 146–151, 2004.

[22] G. M. McFarquhar and A. J. Heymsfield, “Parameterization of tropical cirrus ice crystal size distributions and implications for radiative transfer: Results from CEPEX,” *J. Atmos. Sci.*, vol. 54, pp. 2187–2200, 1997.

[23] E. S. Fleming *et al.*, “Zonal mean temperature, pressure, zonal wind, and geopotential height as function of latitude,” *Adv. Space Res.*, vol. 10, pp. 11–59, 1990.

[24] G. Liu and J. A. Curry, “Topical ice water amount and its relations to other atmospheric hydrological parameters as inferred from satellite data,” *J. Appl. Meteorol.*, vol. 38, pp. 1182–1194, 1998.

[25] L. Froidevaux *et al.*, “Early validation analyses of atmospheric profiles from EOS MLS on the Aura satellite,” *IEEE Trans. Geosci. Remote Sens.*, vol. 44, no. 5, pp. 1106–1121, May 2006.

[26] J.-L. Li *et al.*, “Comparisons of EOS MLS cloud ice measurements with ECMWF analyses and GCM simulations: Initial results,” *Geosphys. Res. Lett.*, vol. 32, 2005. L18710, DOI:10.1029/2005GL023 788.

[27] M. J. Filipiak *et al.*, “Carbon monoxide measured by the EOS Microwave Limb Sounder on Aura: First results,” *Geosphys. Res. Lett.*, vol. 32, no. 14, 2005. L14825, DOI:1029/2005GL022 765.

[28] Q. B. Li *et al.*, “Convective outflow of south Asian pollution: A global CTM simulation compared with EOS MLS observations,” *Geophys. Res. Lett.*, vol. 32, 2005. L14826, DOI:10.1029/2005GL022 762.

[29] G. L. Stephens *et al.*, “The Cloudsat mission and the A-train: A new dimension of space-based observations of clouds and precipitation,” *Bull. Amer. Meteorol. Soc.*, vol. 83, no. 12, pp. 1771–1790, 2002.

[30] H. H. Aumann *et al.*, “AIRS/AMSU/HSB on the Aqua mission: Design, science objectives, data products, and processing systems,” *IEEE Trans. Geosci. Remote Sens.*, vol. 41, no. 2, pp. 253–264, Feb. 2003.

[31] S. Platnick *et al.*, “The MODIS cloud products: Algorithms and examples from Terra,” *IEEE Trans. Geosci. Remote Sens.*, vol. 41, no. 2, pp. 459–473, Feb. 2003.

Dong L. Wu (M’96) received B.S. degree from the University of Science and Technology of China in 1985, the M.S. degree in physics from Louisiana State University in 1990, and the M.S. degree in electrical engineering and the Ph.D. degree in atmospheric science from the University of Michigan, Ann Arbor, in 1993 and 1994, respectively.

He joined the Jet Propulsion Laboratory (JPL), California Institute of Technology, Pasadena, in 1994 to conduct data analyses and algorithm development for the MLS project, and he is currently a Co-Investigator of the EOS MLS experiment. He has authored and coauthored more than 50 papers in peer-reviewed journals on subjects in atmospheric clouds and small-scale gravity waves.

Dr. Wu received the JPL Excellence Award in 1997, the NASA Exceptional Achievement Medal in 2001, and the NASA Board Award in 2005.

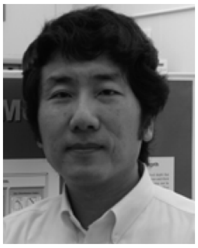

Jonathan H. Jiang received the B.Sc. degree in astrophysics from Beijing Normal University, Beijing, China, in 1985, and the M.Sc. degree in astrophysics and the Ph.D. degree in atmospheric physics from York University, Toronto, ON, Canada, in 1991 and 1996, respectively.

Early in his career, from 1986 to 1988, he taught physics and astronomy at the Nanjing Institute of Technology, Nanjing, China. From in 1989 to 1991, he was with Canada’s Space Astrophysics Laboratory of the Institute for Space and Terrestrial Science and the Centre for Research in Earth and Space Science, York University, from 1992 to 1995, where he was involved, respectively, in the International Ultraviolet Explorer satellite mission and the Canadian Middle Atmospheric Model project. From 1996 to 2001, he was on the research staff and had predoctoral fellowships with McGill’s Centre for Climate and Global Change Research, University of Quebec, Montreal, QC, Canada, and the California Institute of Technology, Pasadena. He also held two part-time physics teaching positions at Trent University, Petersborough, ON, and the University of Waterloo, Waterloo, ON. He joined the Jet Propulsion Laboratory, Pasadena, in 1999, where he is currently a Research Scientist working on the EOS MLS project. His primarily research interests are in radiative transfer modeling, the detection of clouds at microwave frequencies, and the application of MLS data in climate models.

Cory P. Davis received the B.Sc. (Hons,1) and Ph.D. degrees in physics from the University of Otago, Dunedin, New Zealand, in 1996 and 2001, respectively.

He is currently a Postdoctoral Research Fellow with the Institute for Atmospheric and Environmental Science at the University of Edinburgh, Edinburgh, U.K. He is a member of the Microwave Limb Sounding team at this institute and is funded under the NERC Clouds, Water Vapor, and Climate (CWVC) thematic program. His primarily research interest is the influence of Cirrus on EOS-MLS trace gas and cloud property retrievals.